JOURNAL OF PROPULSION AND POWER
Vol. 27, No. 2, March–April 2011

Dynamic Response of Rocket Swirl Injectors, Part II: Nonlinear Dynamic Response

Maksud Ismailov* and Stephen D. Heister†
Purdue University, West Lafayette, Indiana 47907

DOI: 10.2514/1.B34045

Nonlinear boundary element calculations are used to compare and contrast results from the linear theories described in Part I of the study. Parametric evaluations are conducted to assess the influence of vortex chamber dimensions, convergence angle, nozzle length, injector flow rate, and pulsation magnitude on dynamic response characteristics. Resonant frequencies are compared against the linear theory. Overall magnitude of frequency response is characterized for a wide range of injector designs.

Nomenclature

C	=	angular momentum constant, $u_\theta r$
ds_{grid}	=	grid spacing
f	=	disturbance frequency
L_c	=	length of conical convergence section
L_n	=	length of nozzle
L_v	=	length of vortex chamber
$\dot{m}_n$	=	nozzle exit mass flow rate
N_{in}	=	number of tangential inlets
q	=	normal velocity
R_{in}	=	inflow radius, $R_v - R_t$
R_n	=	radius of nozzle
R_t	=	radius of tangential inlet
R_v	=	radius of vortex chamber
r_{he}	=	steady free surface radius at head end
r_n	=	steady free surface radius in uniform nozzle region
r_v	=	steady free surface radius in uniform vortex chamber region
u_θ, u_r, u_z	=	velocity components in circumferential, radial, and axial directions
W_{in}	=	tangential inlet inflow velocity
α	=	angle of solid wall convergence
Δp_{inj}	=	total injector pressure drop
η	=	free surface disturbance
Π_{inj}	=	total injector response
ϕ	=	velocity potential
ω	=	angular disturbance frequency
$()'$	=	fluctuation value of parameter
$\bar{()}$	=	steady-state value of parameter
$\hat{()}$	=	amplitude of fluctuation of disturbed parameter
$()^*$	=	dimensional value of parameter

I. Introduction

IN PART I of this study [1], we developed two analytic/linear models for assessing the magnitude of the injector mass flow pulsation induced by a sinusoidal pressure disturbance on the air core of a classic swirl (simplex) injector. The abrupt convergence resonance model (ACRM) describes the magnitude of injector mass flow response assuming a radial step contraction, while the conical convergence resonance model (CCRM) treats the contraction from the vortex chamber to the nozzle using an arbitrary number of small radial steps. In this second part of the study, numerical calculations are performed to assess nonlinear dynamic response and to compare results with ACRM and CCRM predictions. The vehicle for these computations is a boundary element method (BEM) that preserves surface shapes with high accuracy.

While the community is pursuing nonlinear behavior in numerous free surface problems, there are a comparatively small number of results available for the swirl injector. Notable exceptions to this observation include prior works from our own group [2,3], as well as full Navier–Stokes computations [4]. The prior efforts from our group used an axisymmetric BEM that modeled the inflow tangential channels as an axisymmetric slot of equivalent inlet area. In the present study, this condition is relaxed, and a more natural axisymmetric inflow condition is applied at the head end of the vortex chamber. Using this inflow condition also provides a direct comparison against analytic linear models described in Part I of the study [1]. Parametric studies are conducted to assess the effect of vortex chamber dimensions, contraction angle, nozzle length, and pulsation magnitude over a range of frequencies. Recent experimental work [5,6] provides a strong motivation for the present work, as it clearly depicts evidence of a resonance condition. As evidence, we include the experimental result from this work depicting the frequency response of spray cone angle (Fig. 1). The localized peak at the frequency of about 221 Hz was theorized to be a signal of a resonant mode. For this reason, the geometry used in this experiment served as a baseline for use in the present study. This geometry was provided in Table 2 of Part I of this study [1].

Continuing the discussion on that experimental peak, one would wonder what the existing Bazarov [7] theory would give in its vicinity. Figure 2 shows the answer. There is no peak around 221 Hz, and the closest peak in this area is at 361 Hz; then comes the second peak located further in the higher frequencies, at 726 Hz. Our motivation is to assess the differences between Bazarov's theory, the linear theory developed in Part I of this study [1], and fully nonlinear computations. The following section provides a brief review of the computational tool, followed by results of parametric studies and conclusions from the study.

II. Model Development

Reference [8] provides a complete description of the basic model elements; only highlights will be presented here in the interest of brevity. An inviscid, incompressible, axisymmetric flow is presumed such that the flow dynamics are governed by Laplace's equation, $\nabla^2\phi = 0$. The BEM uses an integral representation of this equation to provide a connection between velocity potential ϕ values on the

Presented as Paper 2010-7137 at the AIAA/ASME/SAE/ASEE Joint Propulsion Conference and Exhibit, Nashville, TN, 25–28 July 2010; received 11 June 2010; revision received 17 September 2010; accepted for publication 3 November 2010.

*Graduate Research Assistant, School of Aeronautics and Astronautics, 701 West Stadium Avenue. Student Member AIAA.

†Professor, School of Aeronautics and Astronautics, 701 West Stadium Avenue. Associate Fellow AIAA.

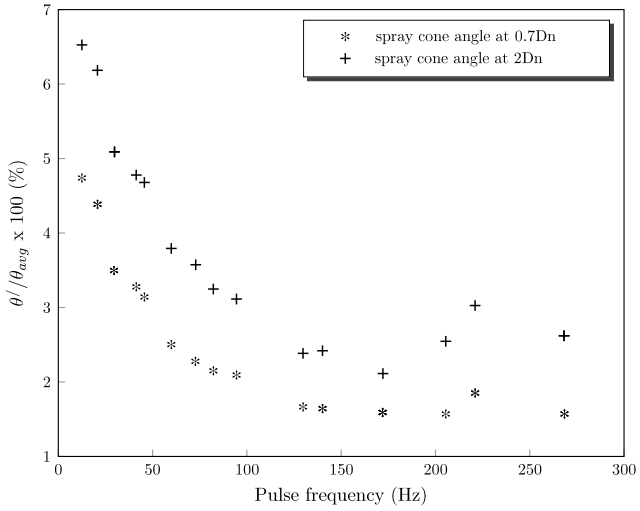

Fig. 1 Experimental data from Ahn [5] (Fig. 6.15) on spray cone angle fluctuation at distances of 0.7 and 2 nozzle diameters from the nozzle exit: peak observed at 221 Hz.

boundary, the local geometry, and the local velocity normal to the boundary, $q = \partial\phi/\partial n$, as follows:

$$c_i\phi(\mathbf{r}_i) + \int_\Gamma \left[\phi\frac{\partial G}{\partial \hat{n}} - qG\right] \mathrm{d}\Gamma = 0 \tag{1}$$

where $\phi(\mathbf{r}_i)$ is the value of the potential at point $\mathbf{r}_i$, Γ is the boundary of the domain, c_i is the singular contribution when the integral path passes over the base point, and G is the free space Green's function corresponding to Laplace's equation. For an axisymmetric domain, the free space Green's function can be expressed in terms of elliptic integrals of the first and second kinds and is a function solely of the instantaneous surface geometry. For this reason, a discrete representation of Eq. (1) can be cast as a linear system of equations relating local ϕ and q values. In the discretization, both ϕ and q are assumed to vary linearly along each element, thereby providing formal second-order accuracy for the method. Since the resulting integrals do not have exact solutions in this case, Gaussian quadrature is used to maintain high accuracy of integration and preserve second-order accuracy overall.

While this governing equation is linear, nonlinearities in these free surface problems enter through the boundary condition at the interface. With regard to the inflow boundary and the solid wall boundary, we can set the normal velocities q exactly. At the inflow boundary, they may be set to their prescribed values as a function of time, and on the solid boundary, they must be zero at all times. Accordingly, the velocity potentials ϕ are the unknowns on these boundaries. The unsteady Bernoulli equation provides a connection between the local velocity potential and the surface shape at any instant in time. Prior formulations [8] have provided a derivation of this result suitable for implementation in a Lagrangian surface tracking environment. For the swirling flow, modifications are required to account for the centrifugal pressure gradient created by the swirl. In the present study, we have made substantive updates to both inflow and free surface boundary conditions, and for this reason, we will provide additional detail here.

A. Boundary Conditions and Computational Mesh

In prior swirl injector simulations by Park [2] and Richardson [3], the tangential inflow was modeled as a cylindrical slot, where the flow enters through its upper cylindrical surface and proceeds radially toward the vortex chamber. The prior inflow condition is contrasted with the current boundary condition in Fig. 3. We choose to introduce fluid axially at the head end of the vortex chamber to better replicate the assumptions of the theoretical models in Part I of the study [1], and because the modeling of the tangential channels is inherently three-dimensional. Physically, the inflow plane would reside just downstream of the tangential inlet holes (a distance of $2R_t$, as shown in Fig. 3), as Bazarov [7] and others have shown that there are slight changes in the free surface in this region due to the conversion from a pure swirling flow to one that also has an axial velocity. The axial velocity q_{in} is defined as

$$q_{\text{in}} = \frac{N_{\text{in}} R_t^2 \bar{W}_{\text{in}}^2}{R_v^2 - [r_1(t)]^2}$$

where N_{in} is the number of tangential inlets, $\bar{W}_{\text{in}} = 1$ is the steady inflow velocity (per the nondimensionalization we employ), r_1 is the radius to the free surface at the inlet plane, and R_v is the radius of the overall vortex chamber. Since the free surface radius r_1 adjusts to balance the overall imposed pressure drop, as we initialize a steady flow, q_{in} will adjust until the free surface is no longer undulating. We define the inflow velocity at this steady-state condition as $\bar{q}_{\text{in}}$. Using this average value over the entire inflow plane, we then impose a sinusoidal oscillation:

$$q_{\text{in}}(t) = \bar{q}_{\text{in}} + q'_{\text{in}}(t) = \bar{q}_{\text{in}}(1 + q_{\text{osc}})\sin(\omega t)$$

where q_{osc} is the amplitude of oscillation.

With regard to the gaseous pressure in the core, linear analyses [9] (Sec. 6.3) show that its action may be noticeable only if the

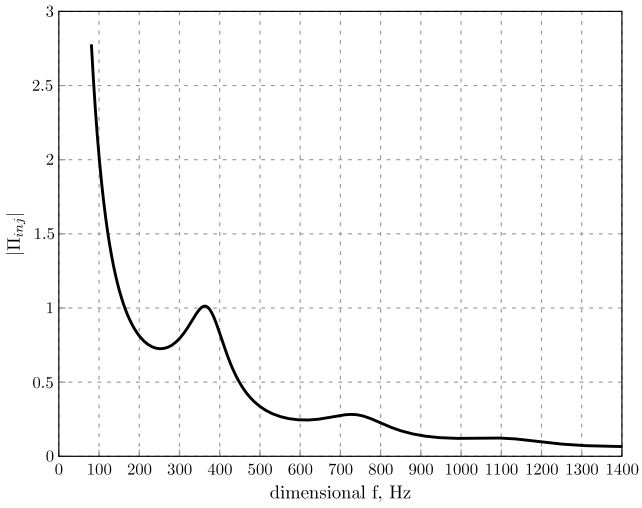

Fig. 2 Response of baseline injector calculated using Bazarov's [7] linear theory: first peak observed at 361 Hz, and second peak observed at 726 Hz.

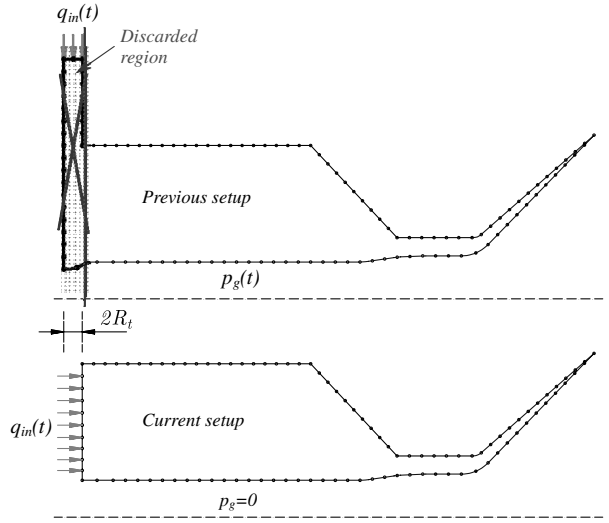

Fig. 3 Schematic of current BEM flow setup compared with prior models by Park [2] and Richardson [3].

gas-to-liquid density ratio is on the order of 10%. We will presume that the overall effect of the surface tension presence is quite weak with regard to the wave dynamics in the vortex chamber and nozzle. Let us generalize these conclusions and assume that we can completely ignore the inertial and capillary effects of the core further on in this study, which allows us to set the gas pressure in the core to zero, $p_g = 0$.

The free surface boundary condition is the most challenging due to the unsteady and swirling nature of the flow. Physically, the free surface boundary condition can be thought of as a local pressure balance where dynamic and static pressure is interchanged (potentially with capillary pressures as well) via the description of an unsteady Bernoulli equation. We cannot see the swirling component of the flow, which is perpendicular to the axial/radial flow plane, yet this portion of the flow imposes hydrostaticlike pressures that must be reflected in the overall dynamic behavior.

Prior implementations by Yoon [10], Park [2], and Richardson [3] introduced a total potential field ϕ_t that is composed of two parts: the first, which describes the movement only in the radial and the axial directions, and the second, which describes the movement only in the circumferential direction. The linearity of the governing Laplace's equation permits a direct superposition of these potentials. The resulting Bernoulli's equation of these authors has included the Rossby number as a dimensionless representation of the swirl level. However, for a dynamic situation, the swirl level, and hence the Rossby number, can vary in time, and an improved treatment was required in order to reflect this fact. For this reason, we employ a slightly different formulation in the present work.

Since angular momentum must be conserved in a potential flow, for an axisymmetric situation, we have

$$\frac{\mathrm{D}}{\mathrm{D}t}(ru_\theta) = \frac{\mathrm{D}C}{\mathrm{D}t} = 0 \tag{2}$$

where $\mathrm{D}/\mathrm{D}t$ is the material derivative, and $C = ru_\theta$ is the angular momentum constant associated with the flow. Since C must be invariant in a Lagrangian sense, the swirl level can change locally as waves convect through the vortex chamber. The overall velocity field is

$$\nabla\phi = [u_r, u_\theta, u_z] = \left[\frac{\partial\phi}{\partial r}, \frac{1}{r}\frac{\partial\phi}{\partial\theta}, \frac{\partial\phi}{\partial z}\right] = \left[\frac{\partial\phi}{\partial r}, \frac{C}{r}, \frac{\partial\phi}{\partial z}\right] \tag{3}$$

where we have used the fact that the circumferential flow component is given by the potential free vortex.

Next, the Lagrangian derivative for the whole flowfield may be written as

$$\frac{\mathrm{D}\phi}{\mathrm{D}t} = \frac{\partial\phi}{\partial t} + \nabla\phi\cdot\nabla\phi \tag{4}$$

In this equation, we know that the Eulerian time derivative is given by the usual unsteady Bernoulli's equation that, since we neglect the gaseous core presence, can be written as

$$\frac{\partial\phi}{\partial t} + \frac{1}{2}\nabla\phi\cdot\nabla\phi = A \tag{5}$$

where A represents the steady-state terms. Without the loss of generality, we can set $A = 0$ by incorporating the steady terms into ϕ. With this, we can rearrange Eq. (5) to

$$\frac{\partial\phi}{\partial t} = -\frac{1}{2}\nabla\phi\cdot\nabla\phi \tag{6}$$

The second term in Eq. (4) can be obtained from Eq. (3) as

$$\nabla\phi\cdot\nabla\phi = \left(\frac{\partial\phi}{\partial r}\right)^2 + \left(\frac{\partial\phi}{\partial z}\right)^2 + \frac{C^2}{r^2} \tag{7}$$

Combining Eqs. (4), (6), and (7), we have

$$\begin{aligned}\frac{\mathrm{D}\phi}{\mathrm{D}t} &= -\frac{1}{2}\nabla\phi\cdot\nabla\phi + \nabla\phi\cdot\nabla\phi = \frac{1}{2}\nabla\phi\cdot\nabla\phi \\ &= \frac{1}{2}\left[\left(\frac{\partial\phi}{\partial r}\right)^2 + \left(\frac{\partial\phi}{\partial z}\right)^2 + \frac{C^2}{r^2}\right]\end{aligned} \tag{8}$$

To get the Lagrangian derivative for the points moving in the two-dimensional BEM plane, which are represented by the velocity potential ϕ_{BEM}, we can subtract the Lagrangian derivative of the swirling component of the flow from the Lagrangian derivative of the total field:

$$\frac{\mathrm{D}\phi_{\mathrm{BEM}}}{\mathrm{D}t} = \frac{\mathrm{D}\phi}{\mathrm{D}t} - \frac{\mathrm{D}(C\theta)}{\mathrm{D}t} \tag{9}$$

The Lagrangian derivative of the swirling component of the flow can be written as

$$\frac{\mathrm{D}(C\theta)}{\mathrm{D}t} = \frac{\mathrm{D}C}{\mathrm{D}t}\theta + C\frac{\mathrm{D}\theta}{\mathrm{D}t} \tag{10}$$

In this expression, we know that the first term is zero due to Eq. (2), and for the second term, we have

$$\frac{\mathrm{D}\theta}{\mathrm{D}t} = \frac{\partial\theta}{\partial t} + \left[u_r, \frac{C}{r}, u_z\right]\cdot\left[\frac{\partial\theta}{\partial r}, \frac{1}{r}\frac{\partial\theta}{\partial\theta}, \frac{\partial\theta}{\partial z}\right] = \frac{C}{r^2}$$

Then, we can rewrite Eq. (10) as

$$\frac{\mathrm{D}(C\theta)}{\mathrm{D}t} = \frac{C^2}{r^2} \tag{11}$$

Substituting Eqs. (8) and (11) into Eq. (9), we obtain

$$\begin{aligned}\frac{\mathrm{D}\phi_{\mathrm{BEM}}}{\mathrm{D}t} &= \frac{1}{2}\left[\left(\frac{\partial\phi}{\partial r}\right)^2 + \left(\frac{\partial\phi}{\partial z}\right)^2 + \frac{C^2}{r^2}\right] - \frac{C^2}{r^2} \\ &= \frac{1}{2}\left[\left(\frac{\partial\phi}{\partial r}\right)^2 + \left(\frac{\partial\phi}{\partial z}\right)^2 - \frac{C^2}{r^2}\right]\end{aligned} \tag{12}$$

To be consistent with the ϕ-q notation for the BEM parameters we have been using so far, we can rewrite the last equation by omitting the BEM index:

$$\frac{\mathrm{D}\phi}{\mathrm{D}t} = \frac{1}{2}\left[\left(\frac{\partial\phi}{\partial r}\right)^2 + \left(\frac{\partial\phi}{\partial z}\right)^2 - \frac{C^2}{r^2}\right] \tag{13}$$

which is the ultimate form employed within the simulation.

Figure 3 also shows a notional computational mesh that is employed. Because the surface in the vortex chamber undulates with time, the grid on the inflow boundary is allowed to compress or expand to fill the instantaneous distance between the vortex chamber wall and the current head-end free surface location. Fixed grid spacing is employed on solid walls. On the free surface, a dynamic grid is used. Using a Lagrangian tracking of the interface points, positions are updated at each instant in time. A spline fit is then applied to the entire free surface, and nodes are redistributed so as to maintain a uniform grid spacing ds_{grid}. Although not shown in the figure, ring-shaped structures are formed due to capillary instabilities on the conical sheet downstream of the nozzle exit. A pinch criteria is employed to shed these structures when nodes on opposing sides of the ligament get within a specified fraction of the overall mesh spacing [11]. Pinching events lead to dynamic changes in the size of the computational mesh. While the pinch criteria are very important when attempting to establish the size of the pinched structures, the emphasis of the present study of the dynamic mass flow production at the nozzle exit makes this criteria of lesser importance, as demonstrated in subsequent grid function convergence studies. Local surface slope and curvature are computed to fourth-order accuracy, and the surface is evolved in time using a fourth-order Runge–Kutta time integration. More details on the free surface treatment can be found from Park [2] and Heister [12].

B. Injector Response Computation

In dynamic system evaluation, the injector response or admittance is often an important consideration. The dimensionless response Π_{inj} describes the level of mass flow pulsation created by a given pressure perturbation:

$$\Pi_{\text{inj}} = \frac{\dot{m}'_n/\bar{\dot{m}}_n}{\Delta p'_{\text{inj}}/\Delta \bar{p}_{\text{inj}}}$$

Because, in our current BEM model, we are analyzing the flow starting from the left end of the uniform vortex chamber region (or from $z = 2R_t$ of the actual injector) and the tangential inlets are out of our consideration (see Fig. 3), the total pressure drop of the BEM injector is equal to the pressure drop through the liquid body at the inflow boundary. The average pressure drop required to establish the swirling inflow can be expressed as

$$\Delta \bar{p}_{\text{inj}} = \rho \frac{C^2}{2}\left[\frac{1}{\bar{r}_1^2} - \frac{1}{R_v^2}\right] \tag{14}$$

where we note that the free surface radius at the inflow boundary r_1 is a function of time when pulsations are present, and its value is averaged over time to give the mean pressure drop. It can be shown [9] (Sec. 7.6) that the unsteady portion of the pressure can be expressed as

$$\Delta p'_{\text{inj}} = \rho \frac{C^2}{\bar{r}_1^3} r'_1 \tag{15}$$

Once a quasi-periodic behavior is obtained, the value for r'_1 can be computed as the difference in maximum and minimum surface heights over a given period of the oscillation.

In principle, the nozzle mass flow $\dot{m}_n$ can be computed as the integral of the axial momentum flux across the film at the exit of the nozzle. However, as the computational mesh does not traverse the film in this region, one needs to compute axial velocities at prescribed interior points, as was done in Richardson [3]. However, this process extends computation times significantly, and the analysis at the curved film boundary at the nozzle exit is not consistent with the assumptions employed in the analysis in Part I of this study [1]. For these reasons, an alternative approach was taken. Rather than use the exact exit plane to measure flow rate histories, we use a point at a distance of one-half nozzle length ($0.5L_n$) from the exit plane, as computations show that the film is very nearly parallel with the injector axis and nozzle wall at this locale. While there is a short time lag between this location and the actual exit plane, the phase shift associated with this lag is small, as the velocities in the nozzle are large, and typical nozzle lengths employed are also quite small. Moreover, this location permits direct comparison against the analytic results developed in Part I of the study [1].

To avoid the inclusion of interior points, the axial velocities on either side of the film at the $0.5L_n$ location are computed using fourth-order centered difference formulas [9] (Sec. 7.6), and a linear axial velocity profile across the film is assumed. In prior work [3], the velocity profiles across the film were shown to be quite linear; in fact, the velocities on either side of the film are nearly identical due to the inviscid nature of the assumed flow. This process permits a streamlined evaluation of the nozzle exit flow that is consistent with assumptions employed in the analytic models from Part I of this study [1].

III. Grid Convergence Study

Four different mesh spacings of 0.06, 0.07, 0.08, and 0.09 were evaluated using the baseline geometry described in Part I of the study [1]. Both steady and unsteady characteristics were evaluated. A dimensionless time step of 0.0005 was used in all simulations. The dimensionless period for the highest frequency disturbances to be evaluated is about 0.5, which implies that we take about 1000 time steps per period for these highest frequencies.

Steady-state surface shapes have shown to be converging for the mesh size of 0.06 [9] (Sec. 7.7). As the unsteady nature of the solution is of primary value here, the overall frequency response of the baseline injector was assessed to evaluate mesh sensitivity. For evaluation of unsteady characteristics, a sinusoidal velocity perturbation of amplitude 30% of the mean inflow velocity was used in all cases. Figure 4 shows the result of this process, indicating an insensitivity in response levels to the four mesh sizes evaluated. The finest mesh spacing of 0.06 was selected, as it was still amenable for use in the computational environment available for the study. A typical run time on a 2.4 GHz processor was roughly 60 h to evaluate response at a single frequency.

IV. Results

Parametric studies were performed to assess the influence of pulsation magnitude, injection conditions, and injector geometry on its dynamic response. Comparisons are made against the analytic models developed in Part I of this study [1]. Specifically, we compare predicted resonant tones from the ACRM, as well as the tones predicted from the CCRM. The baseline injector geometry described in Part I of this study serves as the point of departure for all calculations, and all results assume a 30% pulsation magnitude, except where noted in the pulsation magnitude assessment in the following section. In total, over 1000 individual cases were evaluated for this part of the study.

A. Assessment of Nonlinearity and Choice of Pulsation Magnitude

The effect of the magnitude of the velocity pulsation was addressed in parametric fashion on the baseline injector configuration. Velocity pulsation magnitudes q_{osc} equal to 5, 10, 30, and 50% of the mean injection velocity were considered.

Figure 5 shows the magnitude of the injector responses at various pulsation levels. Overall, the response is very insensitive to pulsation level, indicating that nonlinear effects are of secondary importance. Similar behavior was noted in assessing dynamic response of plain orifice [13] and gas/liquid coaxial [14] injectors.

Figure 6 and Table 1 show the time histories and the average and fluctuation values of the free surface radii r_1 and r_2 (where the latter is the free surface radius at the nozzle center). Perturbations in the surface shape are rather small, even in the case of high-amplitude mass flow pulsations, as the swirl level and axial velocity adjust for the flow rate variation with little response visible on the actual free surface. From Table 1, we can conclude that free surface fluctuation increases roughly linearly with the increase of pulsation magnitude. Figure 7 shows the wave shapes developing in the vortex chamber and the nozzle at different pulsation magnitudes at time $t = 100$. Within the bulk of the vortex chamber, a sinusoidal wave shape is present, but complex shapes evolve in the transition and nozzle regions. For the 5 and 10% pulsation levels, the waves are very small,

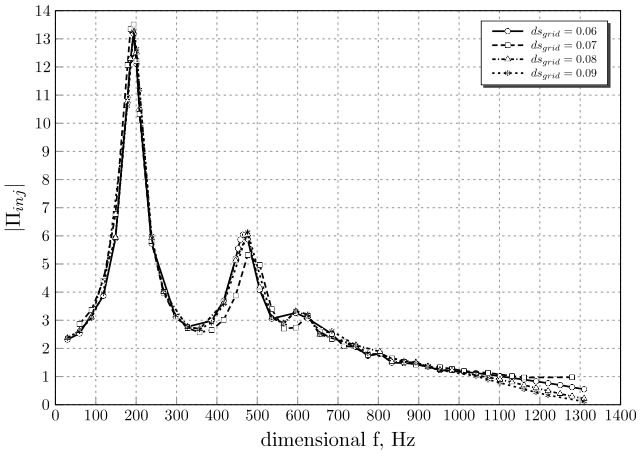

Fig. 4 Injector response sensitivity to grid size variation (baseline injector).

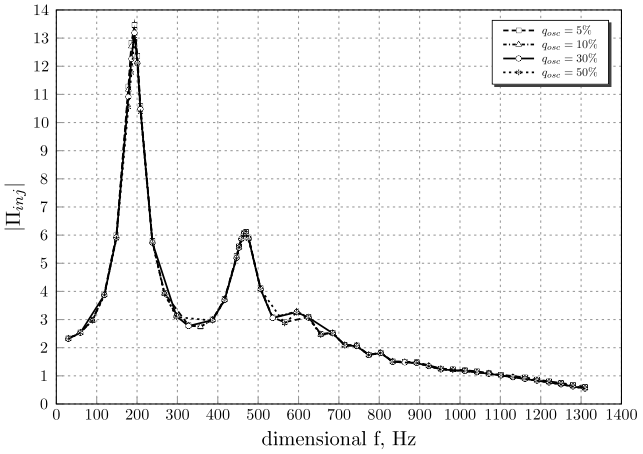

Fig. 5 BEM injector response sensitivity to pulsation magnitude variation (baseline injector).

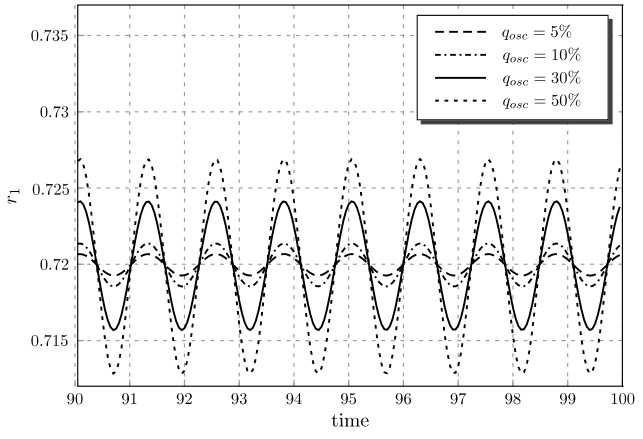

a) Fluctuation of free surface radius at inflow boundary

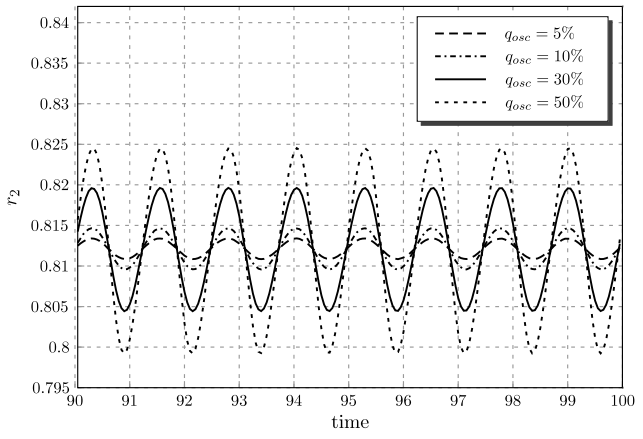

b) Fluctuation of free surface radius at nozzle center

Fig. 6 Stabilized fluctuation of unsteady free surface radii as a function of pulsation magnitude q_{osc} (baseline injector, $f^* = 476.3$ Hz; pulsation started at time $t = 50$).

Table 1 Response of free surface radii r_1 and r_2 to various pulsation magnitudes (baseline injector, $f^* = 476.3$ Hz)

q_{osc}, %	$\bar{r}_1$	r'_1	$r'_1/\bar{r}_1$	$\bar{r}_2$	r'_2	$r'_2/\bar{r}_2$
5	0.7200	0.0007	0.0981%	0.8121	0.0013	0.1579%
10	0.7200	0.0014	0.1961%	0.8121	0.0025	0.3135%
30	0.7199	0.0042	0.5868%	0.8120	0.0076	0.9360%
50	0.7199	0.0070	0.9772%	0.8119	0.0127	1.5588%

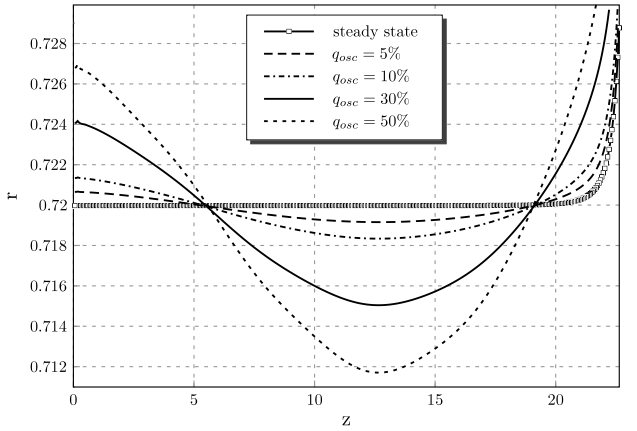

a) Wave shapes in vortex chamber upon uniform steady free surface

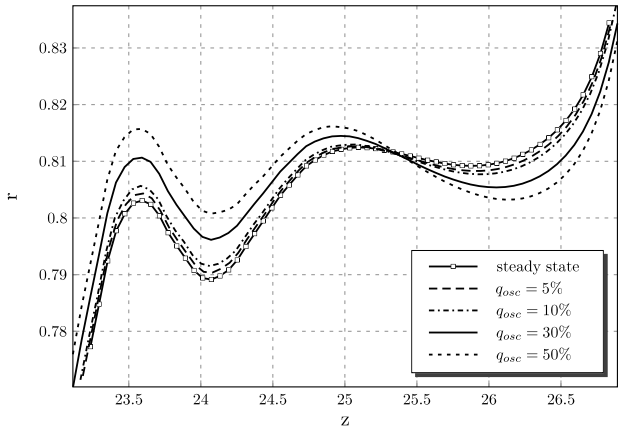

b) Wave shapes in nozzle upon nonuniform steady free surface

Fig. 7 Wave shapes in vortex chamber and nozzle as a function of pulsation magnitude q_{osc} at time $t = 100$ (baseline injector, $f^* = 476.3$ Hz; pulsation started at time $t = 50$).

and assessing statistics relative to mass flow pulsation magnitude can be numerically challenging. In Fig. 7b, we can see that at 30% pulsation, we get a much more distinctive wave shape in the nozzle than at 5 and 10%. For this reason, we chose this pulsation level for use in the remainder of the parametric studies. At the same time, by looking at the time histories of head-end r_1 and midnozzle r_2 radii in Fig. 6, we can conclude that the pulsation can be well described as linear at all considered magnitudes. A question may arise now: why do we get a linear sinusoidal fluctuation of the free surface at pulsation magnitudes as strong as 30 or 50%? These numbers seem large; however, bear in mind that the bulk flow velocity in the vortex chamber is quite small. Thus, the resulting bulk flow pulsation may be considered as quite weak, which results in the linear fluctuation of the free surface, accordingly.

B. Conical Convergence Angle Variation

Variation of the convergence angle α does not have a great influence on the steady-state shape of the free surface [9] (Sec. 3.1). However, as changes in α change the overall length of the injector, we do expect for this parameter to effect the dynamic response of the injector.

Figure 8 depicts the magnitude of the frequency response of the baseline injector with various convergence angles. Strong response is evidenced at primary resonance and at the second harmonic of the resonant frequency. A third harmonic appears weakly for the 60 and 90° cases, but it is absent at lower convergence angles. In general, increasing α tends to shift resonant peaks to higher frequencies, as the overall injector length is shortened as α increases. The heights of the response peaks are not greatly affected until α reaches the 30° case. The long convergent section in this case leads to some destructive

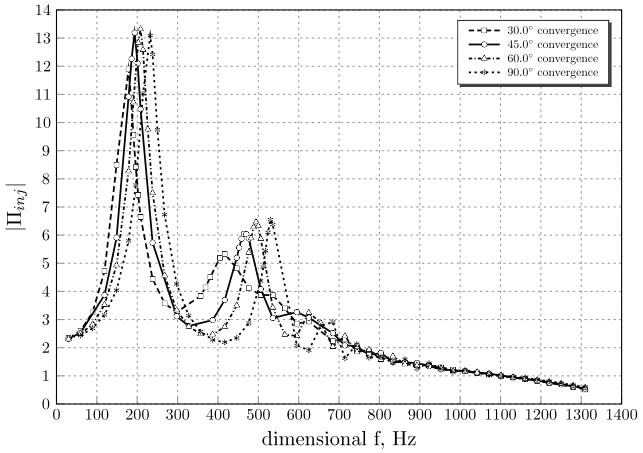

Fig. 8 BEM injector response sensitivity to conical convergence angle variation.

interference in wave patterns, thereby dropping and broadening peaks in the response curve. This factor may also explain the lack of higher-order resonances when α values are below 60°.

Table 2 provides a comparison of computed resonant frequencies with those calculated from the analytic models described in Part I of the study [1]. Since the ACRM assumes a vertical wall at the contraction plane, we use an effective length that includes half of the contraction length to evaluate frequencies and resonance conditions. In contrast, the CCRM does retain α as a parameter. In general, the ACRM is in better agreement with BEM for the primary resonant peak (peak 1 in Table 2), while the CCRM does a better job in matching the higher harmonic (peak 2).

Figures 9a and 9b depict the response levels predicted in the analytic models near the resonant conditions. In Fig. 9a, the ACRM shows a broad peak with a sinusoidal shape in the region near resonance, while BEM results show a much sharper peak. The ACRM does a poor job in replicating the second harmonic, as was noted in Table 2. Figure 9b show the magnitude predicted by the CCRM model. These amplitudes show an even broader character than the ACRM model, as a wider range of frequencies lead to substantial amplitude waves under the CCRM assumptions. While this model does react to the α variation in the same manner as the BEM has shown, the peaks have the overall tendency to shift to the higher frequencies, and the intensity of the outgoing waves a_2 does not exhibit any visible trend.

From Table 2, we can conclude that the ACRM agrees with the first BEM peak relatively well (within 8% in all cases), but it does a rather poor job in replicating BEM results for the second peak. On the other hand, there is an excellent matching of the second peak frequencies of BEM with the CCRM, but there is a rather poor job of matching the primary resonance with this model. The CCRM delivers large refraction waves at higher convergence angles, and the wave interactions are highly complex while the ACRM delivers simpler waveforms. For this reason, the explanation as to why one model matches one peak and one does a better job matching another peak is highly complex and a topic for further work. Lacking a more detailed

Table 2 Resonant peaks for α variation cases (based on Figs. 8 and 9)

α, °	Peaks, Hz	BEM	ACRM	CCRM
30	1	178.6	192.8	116
	2	416.7	578.5	448
45	1	193.5	205.7	118
	2	464.4	617.0	470
60	1	208.4	213.9	120
	2	494.1	641.6	471
90	1	232.2	226.2	n/a
	2	529.8	678.7	n/a

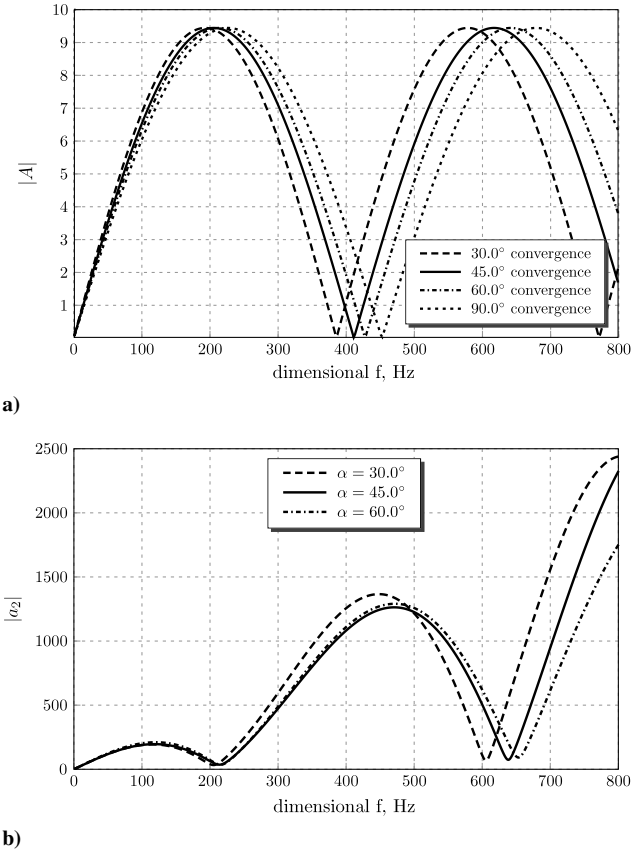

Fig. 9 Sensitivity of resonant peaks predicted by a) ACRM and b) CCRM to conical convergence angle variation.

understanding and the computational resources required for a nonlinear calculation, we recommend using ACRM for primary resonance and CCRM for secondary resonance.

In conclusion, we shall take a moment to recognize that the analytical ACRM and BEM values of the first peak for $\alpha = 45°$ in Table 2, of 205.7 and 193.5 Hz, fall near the experimental peak of 221 Hz in Fig. 1, from which we started the whole discussion in this part of the study. This supports the conclusion that the resonance condition described in Eq. 4 of Part I of this study [1] has some merit in describing the frequency where a locally high injector response could be expected. We also used Bazarov's [7] technique to analyze this experimental condition, and it gives a resonance at a much higher frequency of 361 Hz, assuming a viscous correction value of 0.1. Ideally, we should have had a second experimental peak, with the analytical and computational values we already have in Table 2, to be completely certain in this conclusion.

C. Vortex Chamber Length Variation (90° Convergence Angle)

A series of simulations were carried out to assess the effect of vortex chamber length, $L_v = 5$, 10, 15, and 19, on the response characteristics of the baseline injector geometry using a sharp step convergence from the vortex chamber to the nozzle. Figure 10 and Table 3 show, respectively, the computational BEM results and the frequencies where the BEM and ACRM response curves for each L_v peak out. The CCRM cannot be used here, because a cylindrical section needed to fit into the 90° step transition would be of length zero, which physically collapses the CCRM to ACRM. We can see that the peaks shift to lower frequencies as the vortex chamber length is increased. An analogy here may be drawn with stringed musical instruments. Smaller-sized instruments, like the violin, produce higher pitch sounds than larger-sized instruments, like the guitar or contrabass. As in Sec. IV.B, this is attributed to the fact that the longer vortex chamber naturally selects/generates longer standing waves that are the result of the lower pulsation frequency, and vice versa. We can look at this from the mathematical point of view as well, if we

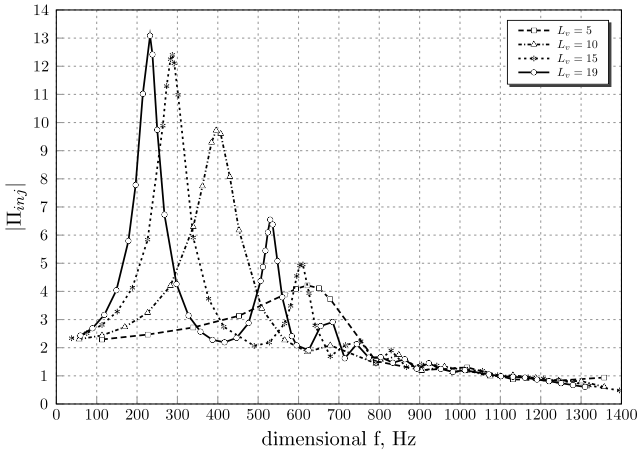

Fig. 10 BEM injector response sensitivity to vortex chamber length variation (90° convergence angle).

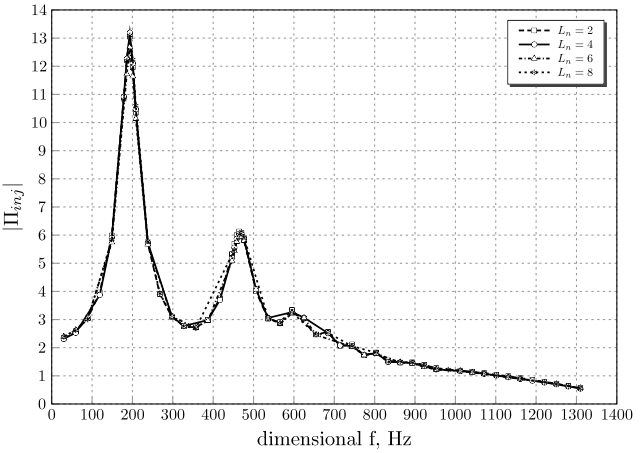

Fig. 11 BEM injector response sensitivity to nozzle length variation (45° convergence angle).

rewrite the equation for the resonant modes from Part I of the study [1] as

$$\omega_0 = n\frac{\pi}{2L_v}\sqrt{C^2\frac{R_v^2 - r_v^2}{2r_v^4}}, \qquad n = 1, 3, 5, \ldots \tag{16}$$

with which the ACRM peaks are calculated in Table 3. From this equation, it becomes clear that the values of the resonant frequencies will decrease as the vortex chamber length is increased. Note, however, that this equation does not provide any information about the amplitude of the oscillation when the injector is at resonance.

The $L_v = 5$ case provides a distinctly different character with a broader peak and no evidence of a second harmonic. In this case, complex wave shapes are obtained, as the nozzle is no longer a negligible length compared with that of the vortex chamber. It is more difficult to sustain a pure standing wave with the short chamber, but substantial amplification is still available in a variety of complex waveforms.

Continuing the discussion on the oscillation amplitudes, in Fig. 10, we can also see that the amplitudes of the peak responses grow larger as the vortex chamber becomes longer. The explanation of physics here may be cast in terms of the spring-damper oscillator, for which the vibration energy is conserved at all times and is given by $E = 0.5m\omega^2A^2$, where m is the mass of the oscillating body, ω is the oscillation frequency, and A is the oscillation amplitude (see discussion in Kinsler and Frey [15], Sec. 1.7). Notice that the mass has the power of one, whereas the frequency has the power of two. Then, we can write the following:

1) The increase in L_v causes proportional linear increase in the mass of the liquid body in the injector's vortex chamber.

2) We know from the preceding that the increase in L_v decreases the peak frequency.

3) In all L_v cases, we excite that liquid mass with the same energy, which is the kinetic energy of excitation $0.5q_{\text{in}}^2$ at the inflow boundary.

4) However, if we have a linear mass increase from one and a quadratic frequency decrease from two, then to conserve the energy of oscillation, the amplitude A should grow in the preceding formula for the energy.

Now, let us compare the frequencies where the peaks are located in the BEM responses and their analytic counterparts. In Table 3, we can see that the ACRM matches the first resonant peak very well for L_v values at or above 10. As mentioned previously, in shorter vortex chambers, the wave pattern cannot be described as a simple standing wave. Also, it is clear that the second resonant peak is far from agreement, which follows the conclusion in Sec. IV.C that the ACRM cannot capture it. On the other hand, the matching of the first resonant peak strengthens the conclusion we have made in the prior subsection, where we said that the ACRM may be successfully used to calculate the first resonant peak in steep angle geometries.

D. Nozzle Length Variation (45° Convergence Angle)

A series of cases were run at nozzle lengths of 2, 4, 6, and 8, using the other dimensions and flow conditions from the baseline injector geometry. Surface shapes were evaluated for steady inflow conditions, and the overall film shapes differed only slightly in the nozzle entrance region for the lengths investigated. The shortest nozzle ($L_n = 2$) did show a slightly different free surface shape in this region, but the longer nozzles were nearly identical. The computed injector responses are shown in Fig. 11, and their peaks, summarized in Table 4, reveal that the overall response is insensitive to the nozzle length. Notice that the $L_n = 2$ response curve looks the same as the others, which tells us that even if the free surface in the nozzle entrance transition region was different in this case, it did not affect the wave reflection/transmission characteristics much.

Theoretically, the deviation of the steady free surface in the $L_n = 2$ case from the rest should affect us in terms of the CCRM, where the point where the transition ends is one of its inputs. Nonetheless, based on the knowledge of response constancy at various nozzle lengths, which we have learned from BEM simulations, and for simplicity, we will assume that it ends at the same $+0.5R_n$ location

Table 3 Resonant peaks for L_v variation cases (based on Fig. 10)

L_v	Peaks, Hz	BEM	ACRM
5	1	622.1	754.1
	2	no data	2262.3
10	1	395.9	411.3
	2	no peak	1234.0
15	1	287.5	282.8
	2	610.8	848.4
19	1	232.2	226.2
	2	529.8	678.7

Table 4 Resonant peaks for L_n variation cases (based on Fig. 11)

L_n	Peaks, Hz	BEM	ACRM	CCRM
2	1	193.5	205.7	118
	2	464.4	617.0	470
4	1	193.5	205.7	118
	2	464.4	617.0	470
6	1	193.5	205.7	118
	2	470.3	617.0	470
8	1	193.5	205.7	118
	2	470.3	617.0	470

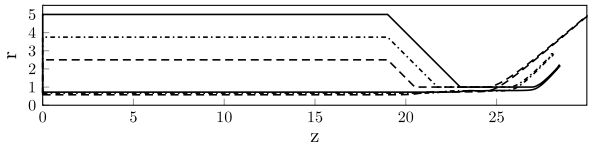

a) General view of considered cases (legend below)

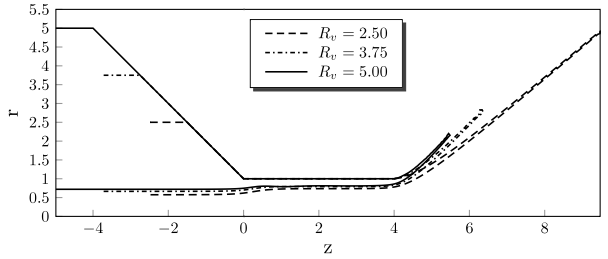

b) Collapsed view of considered cases at nozzle start

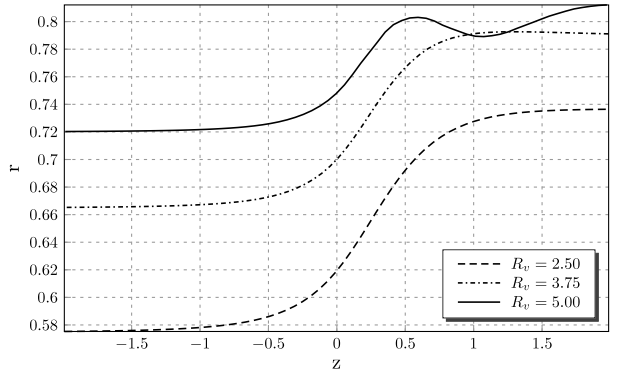

c) Zoomed in view of free surfaces in nozzle entrance transition region

Fig. 12 Steady-state BEM flow boundaries at various vortex chamber radii (45° convergence angle).

with the same radius equal to r_n as the other free surfaces. This allows us to use the same baseline injector results for the analytical peaks in all L_n cases.

Let us now compare the analytical and the BEM peaks with each other. In Table 4, we can see that the BEM computations give nearly the same result for all nozzle lengths. Similarly, ACRM and CCRM values do not vary with nozzle length. As with the convergence angle study, the ACRM result agrees well with the primary peak computed in BEM, while the CCRM better matches the second peak. In general, the nozzle length has little influence on results because of the small amount of time the fluid spends in this region; that is, characteristic frequencies in the nozzle flowpath are much higher than resonant modes determined from chamber characteristics.

E. Vortex Chamber Radius Variation (45° Convergence Angle)

A series of simulations were conducted with differing vortex chamber radii R_v while keeping all other baseline injector geometry and flow conditions the same. The channel inflow velocity was preserved equal to the value described in Part I of the study [1] ($\bar{W}^*_{\text{in}} = 3.7596$ m/s), which implies that the overall pressure drop was varying as we changed the vortex chamber radius.

Figure 12 shows the respective flow geometries. Notice that decreasing the vortex chamber radius leads to a decrease in the core radius and a reduction in the angle of the conical sheet exiting the nozzle. This is due to the fact that the angular momentum, or the swirl strength, becomes smaller, as we have preserved the inflow velocity for all cases. In turn, this allows the swirling fluid to descend to a lower core radius, and because of the greater inertia in the axial direction relative to the baseline case, the fluid is able to discharge further (see similar results in Park [2] (Fig. 4.15).

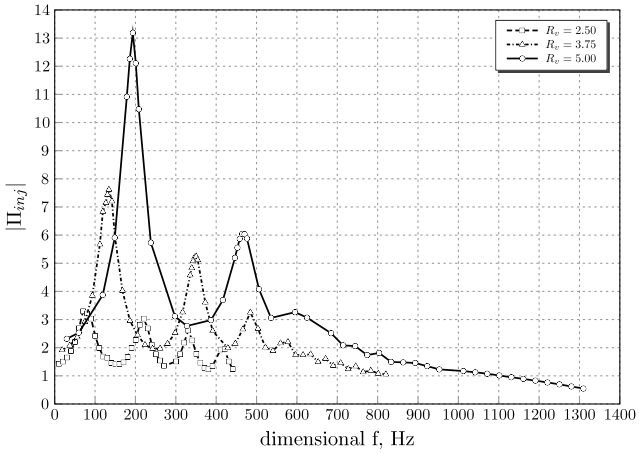

Fig. 13 BEM injector response sensitivity to vortex chamber radius variation (45° convergence angle).

We are more interested in the behavior of the free surface in the transition region. In Fig. 12c, we can clearly see that the transitions in the smaller R_v cases start more upstream and end more downstream of the baseline case. In this study, we consider the following approximations: for the $R_v = 3.75$ case, the transition starts at $-1.0R_n$ and ends at $+1.0R_n$; and for the $R_v = 2.50$ case, the transition starts at $-1.5R_n$ and ends at $+1.5R_n$. Accordingly, the corresponding corrections are made in the inputs for the CCRM.

Figure 13 and Table 5 summarize the frequency response characteristics for the three R_v values considered. In general, the vortex chamber radius has a tremendous effect on the overall response levels, as larger chambers store larger amounts of fluid and become more susceptible to resonance pulsations. As we decrease the vortex chamber radius, the peaks shifts to the left, or to the lower frequencies. In the $R_v = 3.75$ case, we start to see the third harmonic mode. In the $R_v = 2.50$ case, the third mode is very apparent, and the fourth starts to appear. Higher-order harmonics appear to be more pronounced (relative to the primary peak) with the smaller vortex chambers.

Mathematically, the shifting of the peaks to the left can be clearly attributed to the decrease in the swirl strength if we look at Eq. (16), which shows a proportional dependence between the resonant frequency ω_0 and the angular momentum constant C. From the physical point of view, we can say that, as we decrease R_v, the relative increase of the flow momentum in the axial direction, which we mentioned previously, leads to natural elongation of the disturbance waves, which in turn causes the oscillating flow system in the injector to choose the lower resonant frequencies.

Let us now take a look at the results of the analytic resonance models in Table 5. We can see that both the ACRM and the CCRM have captured the preceding BEM trends as we decrease R_v, shifting of the peaks to the lower frequencies. In terms of the actual values of the peaks, however, we can see in Table 5 that the ACRM performed better and located the first two peaks in $R_v = 2.50$ and $R_v = 3.75$ cases. Smaller vortex chambers create more one-dimensional flows, and this may explain why the ACRM begins to agree better with the BEM results as R_v is diminished. In general, the CCRM compares more poorly as R_v is diminished. This may be related to the wrong

Table 5 Resonant peaks for R_v variation cases (based on Fig. 13)

R_v	Peaks, Hz	BEM	ACRM	CCRM
2.50	1	70.2	73.4	no peak
	2	220.5	220.3	162
3.75	1	134.2	132.6	no peak
	2	350.5	397.7	274
5.00	1	193.5	205.7	118
	2	464.4	617.0	470

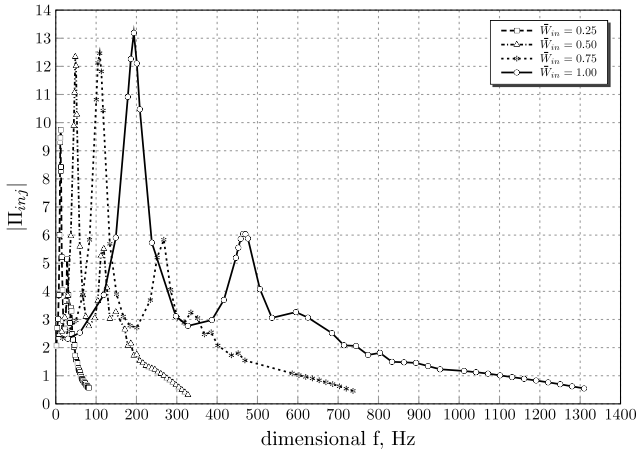

Fig. 14 BEM injector response sensitivity to steady tangential inlet inflow velocity variation (45° convergence angle).

choice of the locations, where we have assumed that the free surface starts and ends its transitioning, or to the fact that, in the smaller R_v geometries, the equations of the long wave fluctuations of the mass flow rate and momentum are not accurately representing the flow disturbances.

F. Flow Rate Variation (45° Convergence Angle)

In this study, we vary the steady inflow velocity $\bar{W}_{\text{in}}$ that, one should note, automatically causes changes in the incoming mass flow rate through $\dot{\bar{m}}_{\text{in}} = N_{\text{in}}\pi R_i^2 \bar{W}_{\text{in}}$ and changes in the swirl intensity through $C = \bar{W}_{\text{in}} R_{\text{in}}$. Varying the flow rate had only minor effects on the overall shape of the free surface, as higher flow is accompanied with higher levels of swirl in all cases. Figure 14 presents the frequency response for several flow rates. Resonant frequencies decrease with decreasing flow rate, and the amplitudes of the peaks decline with decreasing flow rate as well.

The comparison of the peaks in Table 6 reveals that the CCRM has an accurate estimation of the second resonant peaks. Note that the value of R_v in this study was favorable for this model to apply. The ACRM still does reasonably well in capturing the first resonant peak frequency.

G. Comparison of Resonant and Nonresonant Wave Shapes

For this study, we choose a 90° injector with the vortex chamber length of $L_v = 19$, and we consider the free surface motion in the thin region around the mean free surface radius in the vortex chamber over a period of the flow pulsation. During this time interval, we will first present the results for the first resonant frequency of 232.2 Hz (see Table 3) and then the results at a nonresonant frequency that, in this investigation, we have chosen to be 357.2 Hz.

Figure 15a shows the mode shape of the resonant wave pattern revealing a behavior similar to a quarter-wave oscillator with minimal motion near the node at the head end and maximum motion near the nozzle inlet. This quarter-wave resonator shape was postulated in the development of the fundamental condition for

Table 6 Resonant peaks for $\bar{W}_{\text{in}}$ variation cases (based on Fig. 14)

$\bar{W}_{\text{in}}$	Peaks, Hz	BEM	ACRM	CCRM
0.25	1	12.1	12.9	7
	2	27.9	38.6	29
0.50	1	48.4	51.4	30
	2	119.1	154.2	118
0.75	1	108.8	115.7	67
	2	267.9	347.1	265
1.00	1	193.5	205.7	118
	2	464.4	617.7	470

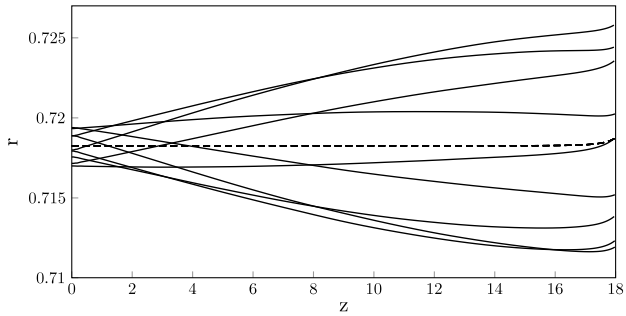

a) First mode resonant wave pattern (f^* = 232.2 Hz)

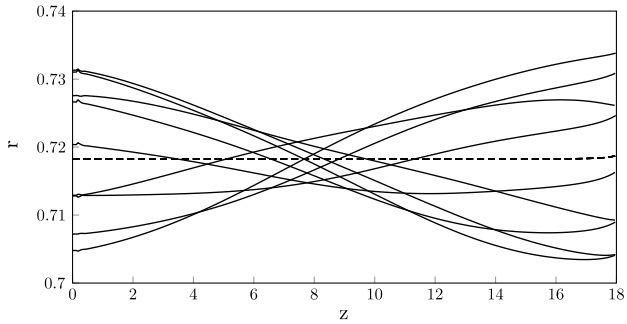

b) Non-resonant wave pattern (f^* = 357.2 Hz)

Fig. 15 Resonant and nonresonant free surface wave envelopes in swirl injector's vortex chamber ($\alpha = 90°$, $L_v = 19$, and $t = 67.6950, \ldots, 70.0950$).

resonance and ACRM model in Part I [1], and it explains the relative success in replicating the primary resonant peaks in the parametric studies. We should note that there is some motion evident at the inflow boundary of the vortex chamber in the simulation results, and this would explain any differences between BEM and ACRM results.

Now, let us take a look at the nonresonant mode shapes in Fig. 15b. The situation is now completely different. We do not have a distinct node or an antinode, and the standing wave behavior is replaced by traveling waves. The node that is apparent is traveling back and forth around the center of the vortex chamber. This reinforces our contention in Part I of the study [1]; when the injector is not at its first resonant mode, the wave pattern in its vortex chamber cannot be described as a standing wave. It is also interesting to note that the wave pulsations are actually larger in magnitude than in the resonant case.

V. Conclusions

The dynamics of the classical swirl injector are highly complex, in that the free surface in the vortex chamber can sustain complex wave shapes due to a combination of reflections and refractions from the convergent surface that forms the nozzle. Large dynamic response can be generated, leading to dimensionless mass flow pulsations many times greater than dimensionless pressure drop perturbations. A resonant condition has been shown to exist wherein the injector behaves as a quarter-wave oscillator, thereby creating large amplitude pulsations at the nozzle that lead to corresponding pulsations in mass flow. The theoretical prediction for this resonant condition (16) agrees quite well with the fully nonlinear calculations over a wide range of injector designs and flow conditions.

We have started this part of the study with the notion that, for the baseline injector, we have one experimental data point for spray cone fluctuation at the pulsation frequency of 221 Hz. We also know from Part I of this study [1] that the ACRM predicts the first resonant frequency of 205.7 Hz, while the nonlinear BEM simulations give a frequency of 193.5 Hz. On the other hand, Bazarov's [7] response curve does not show any extremum in the area of those frequencies. Based on these limited data, there is some evidence that the resonance condition described in this work has merit. Clearly, it would be

desirable to compare the model against other data sets. Bazarov's book contains some high-frequency data he took in the 1970s, but the description of the injector geometries for those tests is incomplete. It is hoped that the present work will motivate some more fundamental experiments for which we can compare the techniques discussed in this study.

The vortex chamber radius has the most prominent effect on injector response, with smaller R_v values leading to smaller response levels at lower frequencies. However, resonances appear to be more pronounced as R_v is decreased. The vortex chamber length also has a strong influence on the levels of injector response, with longer chambers showing higher response levels at lower frequencies. At a very small chamber length ($L_v = 5$ case), we saw a fundamentally different character of response, with sharp well-defined peaks being replaced with a broader peak. The chamber mass flow rate also showed strong influence on the overall response, with higher flow rates leading to larger response levels at higher frequencies.

The nozzle convergence angle α and nozzle length L_n had a much smaller influence on overall injector response. Decreasing α tended to decrease the magnitude of resonant peaks slightly and shift the frequencies to lower values as the overall flowpath length increased with this adjustment. At low values of α, the peaks became less sharp as more complex wave patterns were generated due to the long convergent section. The nozzle length had almost no influence on the results as, for practical designs, even long nozzles are short compared with the vortex chamber length, and the fluid residence time in the nozzle is short due to the high velocities.

The comparison of computational and analytic results is somewhat mixed. The ACRM seems to do a reasonable job in predicting the primary resonance peak for most geometries. In principle, the simple resonant frequency relation (16) provides the designer with a simple mechanism to predict this primary resonance if one uses the length to the midpoint of the convergent section as the equivalent termination of the vortex chamber. Predicting the second harmonic (second peak in the response curve) is more problematic, as neither the ACRM or CCRM results compared consistently well with the BEM calculations over the parameter space investigated. The theoretical resonance in Eq. (16) shows that the second harmonic should be at a frequency three times that of the primary harmonic [i.e., $n = 3$ in Eq. (16)]. If one regards the BEM results as exact and looks at the ratio of the ACRM prediction with BEM calculations, the actual n values vary over the range of $2.2 < n < 3$, based on results in Tables 2–6. As the vortex chamber becomes small, we attain n values closer to the theoretical value of 3.0.

While the CCRM uses more physics, in that it includes a momentum balance as well as a mass balance, it does not replicate the primary resonance frequencies well and had inconsistent agreement with the second harmonics computed from the BEM. We view this as an area of further study, as it is not well understood why such a situation should exist. While the CCRM does seem to have some success in replicating the second resonance peak frequency for a number of different chamber geometries studied, there were also cases with substantial disagreement that cannot be fully explained. In general, analytic models will have difficulty when wave patterns become more complex due to either geometric or input signal variations that lead to additional complexity.

Acknowledgments

This research was supported by the U.S. Air Force Office of Scientific Research and Mitat Birkan under contract number FA9550-08-1-0115.

References

[1] Ismailov, M., and Heister, S., "Dynamic Response of Rocket Swirl Injectors, Part 1: Wave Reflection and Resonance," *Journal of Propulsion and Power*, Vol. 27, No. 2, 2011, pp. 402–411. doi:10.2514/1.B34044

[2] Park, H., "Flow Characteristics of Viscous High-Speed Jets in Axial/Swirl Injectors," Ph.D. Thesis, Purdue Univ., West Lafayette, IN, 2005, Chap. 4.

[3] Richardson, R., "Linear and Nonlinear Dynamics of Swirl Injectors," Ph.D. Thesis, Purdue Univ., West Lafayette, IN, 2007.

[4] Xue, J., "Computational Simulation of Flow Inside Pressure-Swirl Atomizers," Ph.D. Thesis, Univ. of Cincinnati, Cincinnati, OH, 2004.

[5] Ahn, B., "Forced Excitation of Swirl Injectors Using a Hydro-Mechanical Pulsator," Master's Thesis, Purdue Univ., West Lafayette, IN, 2009.

[6] Ahn, B., Ismailov, M., and Heister, S., "Forced Excitation of Swirl Injectors Using a Hydro-Mechanical Pulsator," 45th AIAA/ASME/SAE/ASEE Joint Propulsion Conference and Exhibit, AIAA Paper 2009-5043, Aug. 2009.

[7] Bazarov, V. G., *Liquid Injector Dynamics*, Mashinostroenie, Moscow, 1979.

[8] Park, H., Yoon, S., and Heister, S., "A Nonlinear Atomization Model for Computation of Drop Size Distributions and Spray Simulations," *International Journal for Numerical Methods in Fluids*, Vol. 48, No. 11, 2005, pp. 1219–1240. doi:10.1002/fld.972

[9] Ismailov, M., "Modeling of Classical Swirl Injector Dynamics," Ph.D. Thesis, Purdue Univ., West Lafayette, IN, 2010.

[10] Yoon, S., "A Fully Nonlinear Model for Atomization of High-Speed Jets," Ph.D. Thesis, Purdue Univ., West Lafayette, IN, 2002.

[11] Park, K., and Heister, S., "Nonlinear Modeling of Drop Size Distributions Produced by Pressure-Swirl Atomizers," *International Journal of Multiphase Flow*, Vol. 36, No. 1, 2010, pp. 1–12. doi:10.1016/j.ijmultiphaseflow.2009.09.004

[12] Heister, S., "Boundary Element Methods for Two-Fluid Free Surface Flows," *Engineering Analysis with Boundary Elements*, Vol. 19, No. 4, 1997, pp. 309–317. doi:10.1016/S0955-7997(97)00037-4

[13] McDonald, M., "On the Nonlinear Dynamic Response of Plain Orifice Atomizers/Injectors," Master's Thesis, Purdue Univ., West Lafayette, IN, 2006.

[14] Tsohas, J., "Hydrodynamics of Shear Coaxial Liquid Rocket Injectors," Ph.D. Thesis, Purdue Univ., West Lafayette, IN, 2009.

[15] Kinsler, L., and Frey, A., *Fundamentals of Acoustics*, 2nd ed., Wiley, New York, 1962.

E. Kim
Associate Editor